Journal of Geophysical Research: Atmospheres

RESEARCH ARTICLE
10.1029/2018JD028832

The Life Cycles of Ice Crystals Detrained From the Tops of Deep Convection

Eric J. Jensen[1], **Susan C. van den Heever**[2], **and Leah D. Grant**[2]

[1]NASA Ames Research Center, Moffett Field, CA, USA, [2]Department of Atmospheric Science, Colorado State University, Fort Collins, CO, USA

Key Points:
- Large ice crystals fall out of anvil cirrus within a few hours
- Small ice crystals grow by deposition of vapor
- Ice crystal growth extends lifetime of anvil cirrus

Correspondence to:
E. J. Jensen,
eric.j.jensen@nasa.gov

Citation:
Jensen, E. J., van den Heever, S. C., & Grant, L. D. (2018). The life cycles of ice crystals detrained from the tops of deep convection. *Journal of Geophysical Research: Atmospheres*, *123*, 9624–9634. https://doi.org/10.1029/2018JD028832

Received 13 APR 2018
Accepted 26 JUL 2018
Accepted article online 7 AUG 2018
Published online 6 SEP 2018

Abstract Extensive anvil cirrus clouds generated by deep convection have important impacts on the Earth's radiation budget and climate. We use growth-sedimentation trajectory calculations to investigate the life cycles of anvil ice crystals as they are advected downwind from their convective source. Temperature, water vapor, and wind fields from a cloud-resolving model simulation of an isolated cumulonimbus cloud are used to drive the calculations. Ice crystals are initialized in the main upper-level detrainment zone with a size distribution based on in situ measurements made in a convective core at about 12 km. Advection, deposition growth, and sedimentation of thousands of sample ice crystals are tracked over about 2.5 hr; neither aggregation of ice crystals nor radiative effects are included. Results support the importance of deposition growth and gravitational size sorting in the evolution of the anvil cirrus. Most ice crystals initialized with maximum dimensions larger than about 200 μm fall out of the anvil and sublimate in subsaturated air below within about 2 hr. Few small ice crystals are present in the lower part of the mature anvil. Vapor deposition growth accounts for about 50% of the ice mass remaining after about 2 hr. Ice crystals larger than about 50 μm in the mature anvil have grown substantially by deposition of vapor. This result is consistent with the predominance of bullet rosette habits observed in mature anvils. Variations in ice crystal fall speeds and growth rates associated with ice crystal habit assumptions have little impact on the ice crystal life cycles.

Plain Language Summary Numerical simulations of anvil cirrus ice crystal life cycles demonstrate the importance of deposition growth and sedimentation. Ice crystals with maximum dimensions larger than about 200 μm fall out of anvil cirrus within a few hours. Most ice crystals persisting in the anvils grow by deposition of vapor, and ice crystal growth is important for maintenance of the anvil ice mass. These results are consistent with the predominance of bullet rosette habits observed in mature anvil cirrus.

1. Introduction

Cirrus clouds cover 20–30% of the tropics at any given time (Liou, 1986), and they have a large impact on the Earth's radiation budget, both in terms of the solar flux reaching the surface and the longwave radiation escaping to space. Detrainment of ice and water vapor from deep convection, along with dynamical forcing associated with the deep convection, are responsible for much of the tropical cirrus (Massie et al., 2002; Riihimaki et al., 2012). Hereafter, we refer to cirrus directly produced by deep convection as *anvil cirrus*. Solar and infrared radiative forcings associated with anvil cirrus can be on the order of 100 W/m^2 (Kiehl & Ramanathan, 1990). Tracking of anvil cirrus features in geostationary satellite imagery has been used to show that these clouds can sometimes persist for 12 hr or more (Luo & Rossow, 2004; Mace et al., 2006), and large anvil shields are readily apparent in satellite imagery. Understanding anvil cirrus physical processes is important for both weather forecasting and climate.

The simplest model of anvil cirrus formation involves ice crystals detrained from the upper parts of deep convection cores spreading laterally to generate an extensive cirrus layer. The spreading can be driven by divergence at the tops of the convective updrafts and/or by wind shear, with the latter mechanism generally creating more extensive anvils. As noted by Mace et al. (2006), moderately large ice crystals detrained from deep convection will fall out of the upper troposphere within a few hours, and maintenance of anvil cirrus for several hours or more requires dynamical forcing as well as fresh nucleation of ice crystals and/or growth of small crystals from the convection. Observations of ice crystal habits in anvil cirrus freshly detrained from convective cores (i.e., ages less than an hour or two) indicate primarily pristine crystals and large

(maximum dimensions greater than 100 μm) aggregates (Gallagher et al., 2012), whereas the measurements in high-altitude, aged anvil cirrus downstream of deep convection indicate a predominance of bullet rosette habits (Whiteway et al., 2004; (Woods and P. Lawson, personal communication, June 2017)). At lower altitudes and in electrified continental storms, aggregates can predominate even in aged anvil cirrus (Connolly et al., 2005; Field et al., 2006). The conceptual model we have in mind here is that large aggregates rapidly fall out of the freshly detrained anvil cirrus leaving behind small crystals that subsequently grow into bullet rosettes. Aggregation of ice crystals does occur as they fall through deep anvil cirrus, and images of aggregates are observed in anvil cirrus as noted above. However, at least in the upper parts of the cirrus, bullet rosettes seem to dominate the ice crystal population. (Note that the in situ measurements only provide habit information for ice crystals with maximum dimensions larger than about 40 μm.) Since bullet rosettes are formed by in situ growth in upper tropospheric conditions, these observations suggest that deposition growth is likely an important process for maintaining the ice mass in the upper parts of aging maritime anvil cirrus.

The central issue addressed in this paper is the life cycle of ice crystals detrained from deep convection. In particular, we address the impacts of sedimentation, vapor deposition growth, and sublimation on the temporal evolution of the sizes of anvil ice crystals and the overall anvil ice mass. We use Lagrangian tracking of individual ice crystals, including the processes of advection, sedimentation, growth by deposition of water vapor, and sublimation. Neither aggregation of ice crystals nor the effects of radiation on anvil dynamics and ice crystal growth are included. The ice crystal life cycle calculations are driven by temperature, humidity, and wind fields from a cloud-resolving model (CRM) simulation of an isolated convective system in a sheared environment. These calculations should indicate the life cycles of detrained ice crystals with different sizes, as well as the tendency for growth or sublimation of ice crystals in the aging anvil.

The paper is organized as follows: Section 2 describes the CRM simulation used to drive the Lagrangian calculations, the specifications of ice crystal fall speeds and deposition growth rates, and the initialization of the simulated ice crystal sizes. The results are presented in section 3, and a summary and discussion are provided in section 4.

2. Ice Crystal Growth-Sedimentation Trajectories

The intent here is to track the sizes and locations of individual ice crystals detrained from deep convection. (In the remainder of the paper, we refer to these as simulated ice particles [SIPs]). Since observations cannot provide the full three-dimensional time evolution of temperature, water vapor, and wind fields in an evolving deep convection system, we turn to CRM simulations (see section 2.1). The three-dimensional temperature, relative humidity, and wind fields from the Eulerian CRM are stored at a time resolution of 1 min, and these fields are then used to drive the Lagrangian ice crystal simulations. We initialize the SIPs in the upper parts of the simulated convective system at an early stage in the anvil formation (see section 2.3), and we track their advection, deposition growth/sublimation, and sedimentation. The interaction between the CRM and Lagrangian models is passive; that is, we do not modify the CRM humidity fields in response to the calculated SIP growth and sublimation. Note that in the Regional Atmospheric Modeling System (RAMS) simulation described below, full interaction between the simulated hydrometeors and the vapor/temperature fields is included.

2.1. Cloud-Resolving Model Simulation of an Isolated Cumulonimbus Cloud

The idealized CRM simulation of an isolated tropical cumulonimbus storm was performed with the RAMS (Cotton et al., 2003; Saleeby & van den Heever, 2013), version 6.1.18. In order to capture the full evolution of the anvil, the simulation was integrated for 4 hr. The horizontal and vertical grid spacings were 250 and 100 m, respectively (note that the vertical grid spacing was constant throughout the model depth), and the time step was 1 s. The domain size was 200 km in the east-west direction, 150 km in the north-south direction, and 24.7 km deep for a total of 801 × 601 × 248 grid points. Model output was saved once every simulation minute. An idealized approach was utilized for the isolated cumulonimbus simulation. The initial profiles of temperature, humidity, and winds were applied horizontally homogeneously throughout the domain. The initial sounding was derived from the Grant and van den Heever (2014a) study of idealized tropical sea breeze convection, specifically, from the spatially averaged conditions ahead of the sea breeze at 1700 local time in the control simulation. This sounding is representative of typical tropical environmental conditions. The mixed-layer convective available potential energy associated with this sounding is 1,622 J/kg, where the mixed-layer depth is taken to be 500 m. The wind speed increases with height up to 11 km above ground level

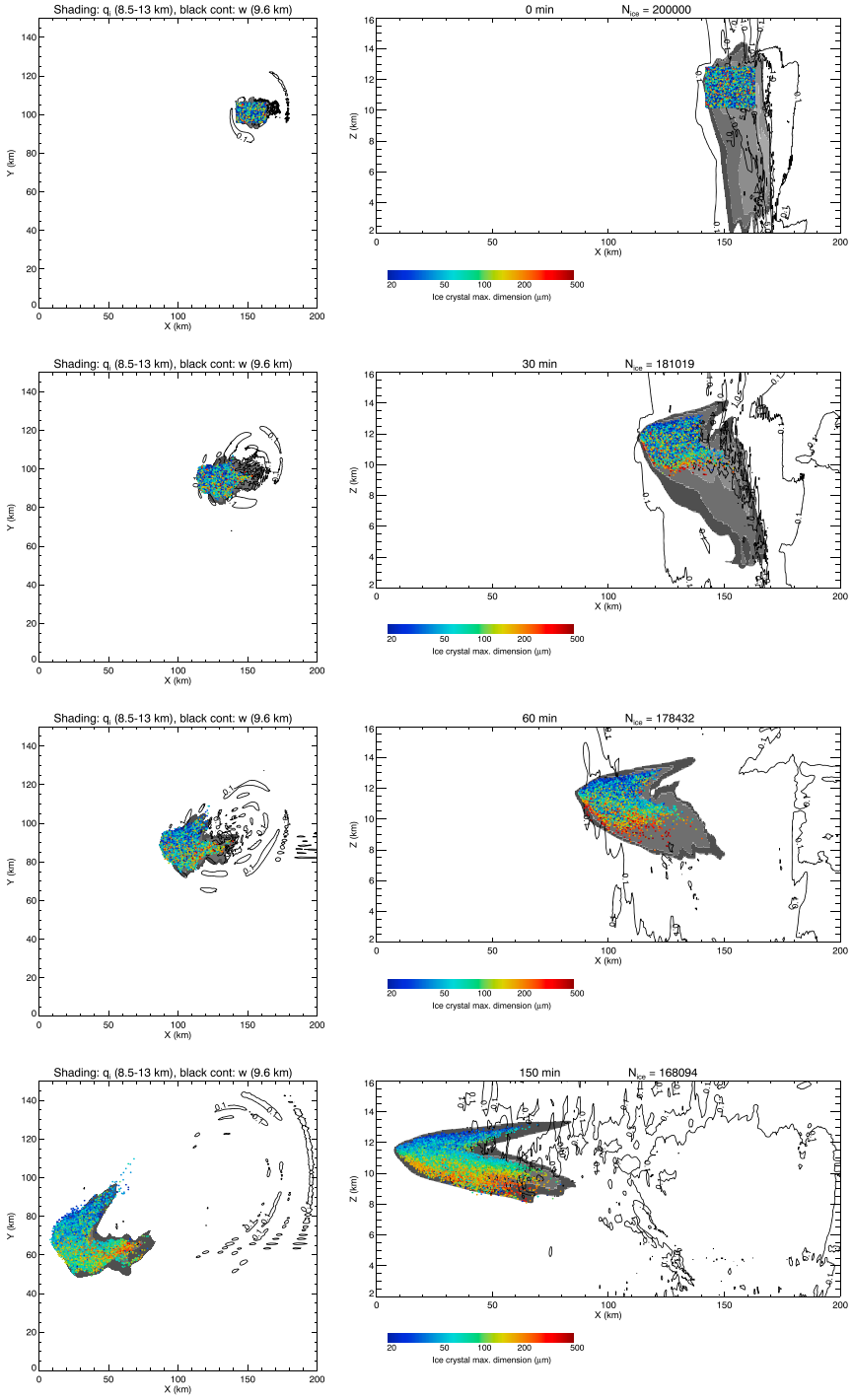

Figure 1. The RAMS ice mixing ratio (gray scale shading, contour levels ranging from 0.0001 to 0.01 g/g), vertical wind speeds (black contours, contour levels of 0.1, 1, and 5 m/s), and Lagrangian simulated ice crystals (color dots) are shown at the time the ice crystal trajectories were initialized (first row) and three subsequent times (second to fourth rows). The color of the dots corresponds to the SIP maximum dimensions, as indicated by the legend. Note that the Lagrangian calculations were initialized at 1816 local time in the RAMS simulation, which we define as zero time in the Lagrangian simulation. (left column) *x*-*y* view with the RAMS ice mixing ratio averaged between 10 and 12 km AGL, and the vertical wind speed shown at 9.6 km AGL. (right column) *x*-*z* view with the RAMS ice mixing ratio averaged across the *y* coordinate, and the maximum value of the vertical wind speed shown. The Lagrangian simulated ice crystals are initially placed randomly within the rectangular volume (first row). Note that only 1 in 20 of the SIPs are shown here. SIP = simulated ice particles; RAMS = Regional Atmospheric Modeling System; AGL = above ground level.

and is northeasterly throughout most of the troposphere. Other parameterizations utilized for the idealized cumulonimbus simulation here include the Smagorinsky (1963) anisotropic subgrid turbulence scheme with stability modifications by Hill (1974), Klemp and Wilhelmson (1978) open radiative boundary conditions, and a Rayleigh damping layer over the topmost 4 km. Radiative transfer, surface fluxes, and Coriolis effects were not included.

Microphysical processes were represented with the two-moment version of the RAMS microphysics scheme, which includes eight hydrometeor categories and prognostic aerosol fields (Meyers et al., 1997; Saleeby & Cotton, 2004; Saleeby & van den Heever, 2013). Two small aerosol modes, one of sulfates and one of dust, were included. The two aerosol species both had median radii of 0.05 μm and were initialized horizontally homogeneously but with a vertically varying profile. The aerosol profile was well mixed throughout the lowest 1 km with a mixing ratio of 1,000 mg^{-1}, and it decreased exponentially above 1 km with a scale height of 500 m. Aerosol particles were advected and diffused, depleted through cloud drop and ice nucleation, sedimentation, and dry deposition, and regenerated via hydrometeor evaporation. Ice nucleation was parameterized following DeMott et al. (2010). While the microphysical and dynamical processes in the RAMS simulation would be altered by using a different specification of aerosol properties, aerosol-cloud interactions are not the focus of this study.

In order to initialize the cumulonimbus cloud, a convergence zone was used following the methodology of Loftus et al. (2008) and Schumacher (2009), except that the convergence zone was implemented as tendencies to the *u* and *v* wind fields. The convergence zone had a 5-km horizontal radius, was centered 30 km from the east edge and 45 km from the north edge of the domain, and was strongest at the lowest model level but decreased linearly in strength up to an altitude of 1 km above ground level. The convergence zone tendency was applied using an amplitude of 4×10^{-3} s^{-1} and a time scale of 15 min. After 30 min, the simulated convergence field closely matches the spatial structure and magnitude of convergence associated with the sea breeze in the Grant and van den Heever (2014b) control simulation.

The evolution of the simulated deep convection and associated anvil cirrus is evident in Figure 1. After $\simeq$1 hr of simulation time, the developing convective updraft forced by the convergence field has reached the tropopause. Subsequent detrainment upon reaching the tropopause produces the cirrus anvil which extends to the southwest in response to the environmental shear. Following the weakening and eventual dissipation of the convective core, the convective detrainment feeding the anvil is reduced. Furthermore, the anvil is no longer anchored to the updraft and is subsequently advected downstream. The reduction in convective core detrainment, together with ice particle sedimentation, results in a significant thinning of the cirrus anvil.

2.2. Ice Crystal Fall Speeds and Vapor Deposition Growth Rates

In the Lagrangian model framework, we follow the traditional approach of calculating ice crystal terminal fall speeds using a relationship between the Best number and the Reynolds number (Mitchell, 1996; Mitchell & Heymsfield, 2005; Pruppacher & Klett, 1997). The modified power law relationship given by Heymsfield and Westbrook (2010) is used. The modified Best number is calculated given the ice crystal maximum dimension, cross-sectional area, and mass, as well as properties of the atmosphere. Then the Reynolds number is calculated using the power law relationship, and the ice crystal fall speed can be calculated from the Reynolds number. Heymsfield and Westbrook (2010) adjusted the dependence of Best number on particle dimensions to provide good agreement with laboratory, wind tunnel, and field measurements.

Ultimately, the ice crystal fall speeds predicted by this approach depend on the assumptions about ice crystal habits, which are generally represented by mass- and area-dimensional power laws:

$$m = \alpha D^{\beta} \tag{1}$$

$$A = \gamma D^{\sigma} \tag{2}$$

where D is the crystal maximum dimension. We use the values for α, β, γ, and σ given by Mitchell (1996) and Heymsfield et al. (1998) for bullet rosettes and aggregates, respectively (see Sölch & Kärcher, 2010, Table AII) to span the range of habit possibilities for ice detrained from deep convection.

Westbrook and Sephton (2017) recently evaluated the fall speeds calculated with the Heymsfield and Westbrook (2010) parameterization by comparison with laboratory measurements using 3-D-printed analogs of ice crystal habits including bullet rosettes and aggregates. The results showed good agreement (fall speeds within about 20% and no systematic bias) for Reynolds numbers relevant for this study.

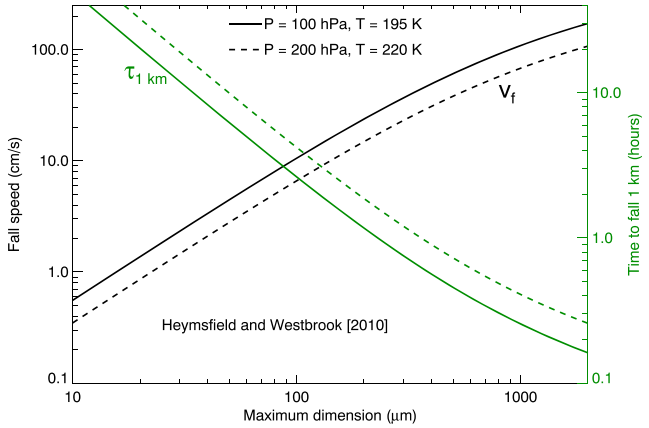

Figure 2. Ice crystal terminal fall speeds (black curves, left axis) based on expressions given by Heymsfield and Westbrook (2010) and the corresponding time to fall 1 km (green curves, right axis) are shown for tropical upper tropospheric conditions (100 hPa, 195 K: solid curves; 200 hPa, 220 K: dashed curves).

Westbrook (2008) showed that the above approach for estimating ice crystal fall speeds can lead to overestimates for small crystals ($D < 100$ μm, $Re < 1$). He used a capacitance-based approach to derive fall speeds for Reynolds numbers less than unity:

$$v_f = \left(\frac{g}{6\pi\eta_a}\right)\frac{m}{C} \tag{3}$$

where the capacitance, C, is essentially the hydrodynamic radius of the ice crystals, g is the acceleration due to gravity, and η_a is the dynamic viscosity. Capacitances for a variety of ice crystal habits were derived by Westbrook et al. (2008). Heymsfield and Westbrook (2010) compared their fall speed calculations with the Westbrook et al. (2008) approach and noted agreement within 30% for small ice crystals.

The dependence of terminal fall speeds calculated from the Heymsfield and Westbrook (2010) approach on crystal maximum dimension is shown in Figure 2 for pressure levels of 100 and 200 hPa, assuming tropical tropospheric conditions. Also shown are the corresponding times for the ice crystals to fall 1 km, which range from tens of hours for ice crystals smaller than about 50 μm to about 10 min for crystals larger than 1 mm.

We also use the standard capacitance approach for calculation of ice crystal diffusional growth (Pruppacher & Klett, 1997), with the capacitance for bullet rosettes and aggregates as specified above. Ice growth can be enhanced by vapor flux driven by the sedimentation of ice crystals. This effect is accounted for with the ventilation factor, f_v, which is generally expressed as a function of $X = Sc^{1/3}Re^{1/2}$, where Sc is the Schmidt number and Re is the Reynolds number. We adopt the parameterization provided by Heymsfield (1975) for bullet rosettes:

$$f_v = 1.0 + 0.3005X - 0.0022X^2 \tag{4}$$

As shown below, the ventilation effect has negligible impact on the results presented here.

The deposition growth calculations used here are based on the assumption that the ice crystal surface temperature is equal to the ambient temperature. However, when the ice saturation ratio is near unity, radiative heating (near cloud base) or cooling (near cloud top) can modify the crystal temperature and significantly affect growth or sublimation rates (Ramaswamy & Detwiler, 1986; Stephens, 1983; Wu et al., 1999). Radiative effects are crystal size dependent, and they tend to broaden size distributions in the upper cloud layers where cooling prevails and narrow size distributions in the lower cloud layers where heating prevails. The effects can be quite complex, and simulations of particular cirrus cases suggest that the overall evolution of the clouds can be significantly affected. Radiative heating can also drive small-scale circulations and turbulence within

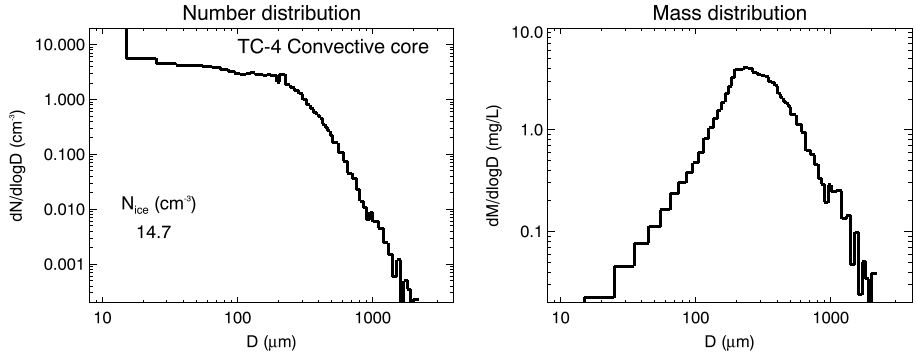

Figure 3. Number and mass distributions derived from two-dimensional stereo measurements in a convective core at about 12 km (Jensen et al., 2009). Large numbers of relatively small (maximum dimension less than 100 μm) ice crystals, as well as large graupel particles, are present in the convective core. TC-4 = Tropical Composition, Cloud and Climate Coupling Experiment.

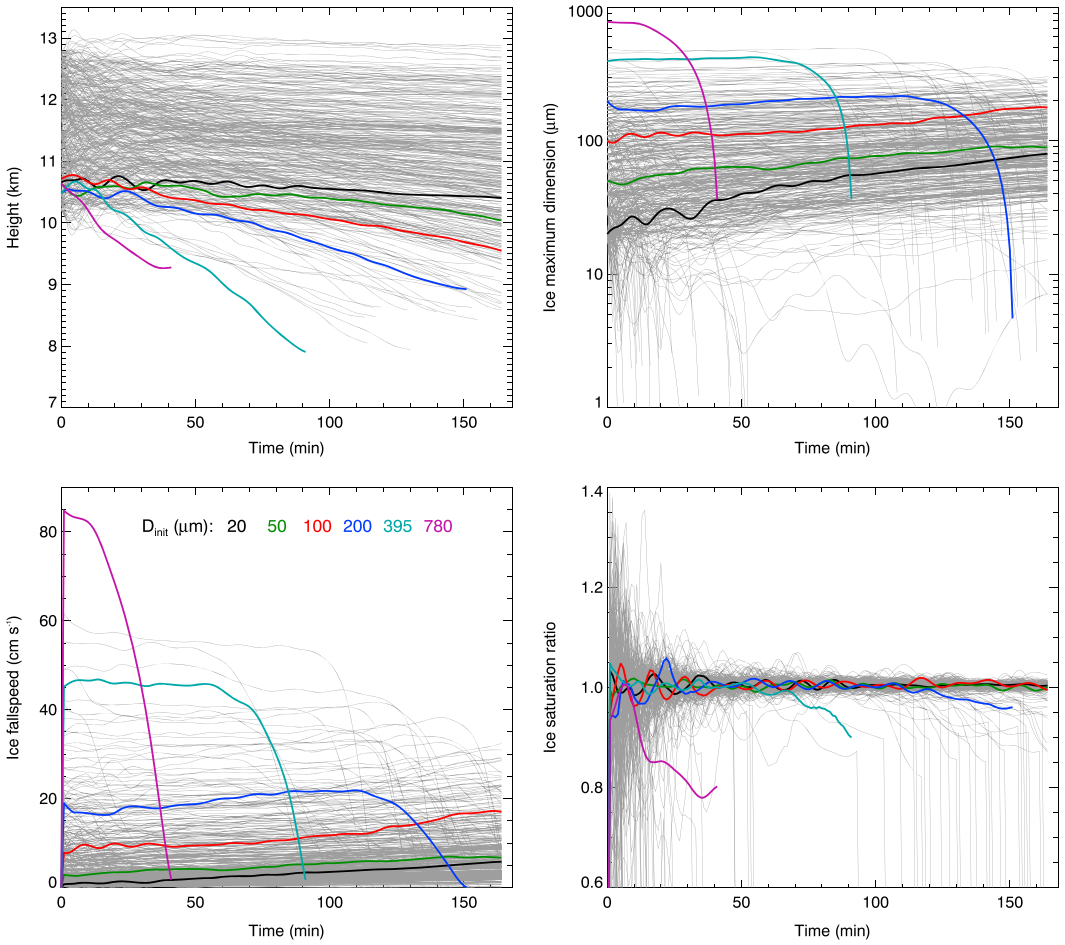

Figure 4. The heights, maximum dimensions, fall speeds, and ice saturation ratios of individual ice crystals are plotted as a function of time. The gray curves show every 500th tracked ice crystal, and the colored curves show representative examples with initial maximum dimensions of 20, 50, 100, 200, 395, and 780 μm. Ice crystals larger than about 200 μm generally fall into subsaturated air below cloud base and sublimate within an hour or two. Sedimentation speeds of crystals smaller than about 50 μm are too slow to appreciably change the ice crystal heights within a few hours. Ice crystals remaining within the primary anvil layer tend to experience moderate supersaturation and grow by vapor deposition. Gravity waves forced by the convection cause oscillations in ice saturation ratio.

the anvils. Since radiative effects were not included in the RAMS simulation used here, we also omit radiative effects on growth/sublimation of ice crystals in the Lagrangian calculations. Anvil radiative effects are likely negligible in the first 30 min of the simulation when gravity waves are driving supersaturations and subsaturations. Radiative heating would likely accelerate the sublimation of ice crystals at cloud base. These issues are the subject of a follow-on study.

We calculate ice crystal fall speeds and diffusional growth rates using either the bullet rosette or aggregate expressions given above to span the range of possibilities. It is no doubt unrealistic to use aggregate habits for small crystals, but we use this approach to span the range of fall speed possibilities. For the baseline case, we assume that the ice crystals are aggregates, Heymsfield and Westbrook (2010) fall speeds are used, and ventilation effects are ignored. Sensitivity experiments using bullet rosettes instead of aggregates, with the Westbrook (2008) fall speeds for crystals smaller than 100 μm, and with ventilation effects included are also discussed.

2.3. Initialization of Simulated Ice Crystals

The 200,000 SIPs are initialized in the main upper-tropospheric detrainment altitude range (10.2–12.8 km) and approximately within the cloud horizontal domain as indicated by the RAMS fields at 1816 local time.

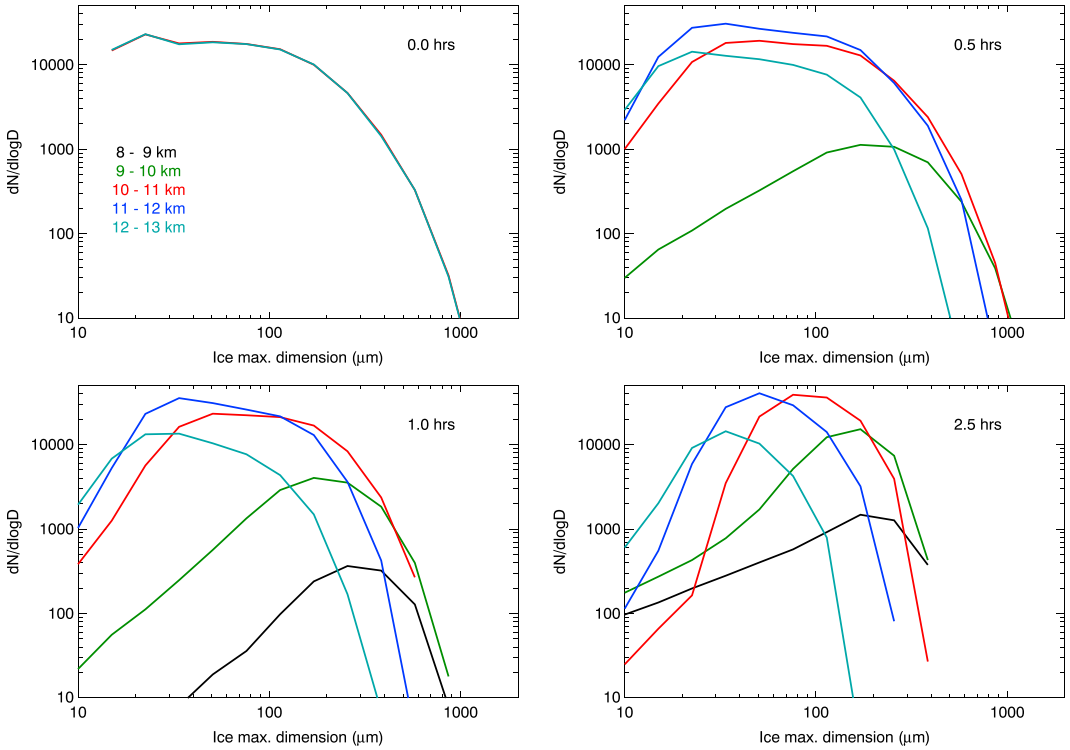

Figure 5. Ice crystal size distributions are shown in 1-km height bins at four times. Gravitational size sorting develops quickly such that about 1 hr after simulated ice particles initialization the anvil is clearly stratified by crystal size.

Specifically, the SIPs are given random locations within the domain $x = 142–163$ km, $y = 96–106$ km, and $z = 10.2–12.8$ km (Figure 1, first row).

For initialization of the SIP sizes, we use in situ measurements made during an aircraft passage through a convective core. During the Tropical Composition, Cloud and Climate Coupling Experiment (TC-4; Toon et al., 2010), the NASA DC-8 inadvertently flew through a strong convective updraft core at about 11–12 km (−47 °C) with a maximum updraft speed of about 20 m/s (Jensen et al., 2009). The two-dimensional stereo measurements during the passage through this core provided unique information about the ice crystal size distribution in convective updrafts. As shown in Figure 3, abundant small (maximum dimension less than 100 μm) crystals were present (ice concentrations greater than 10 cm^{-3} after correction for shattering artifacts). The large numbers of small ice crystals are expected from homogeneous freezing of droplets and aqueous aerosols driven by the strong updraft (Jensen & Ackerman, 2006; Kärcher & Siefert, 2016). Graupel particles with sizes on the order of 1 mm were also lofted to the tops of the convective core. The initial sizes of the SIPs are specified for consistency with the size distribution shown in Figure 3. The TC-4 data are available on the NASA Earth Science Project Office archive (https://espoarchive.nasa.gov/). Our intent here is to simulate a realistic deep convection system with a typical preconvection tropical sounding and the best available information about convective core microphysical properties.

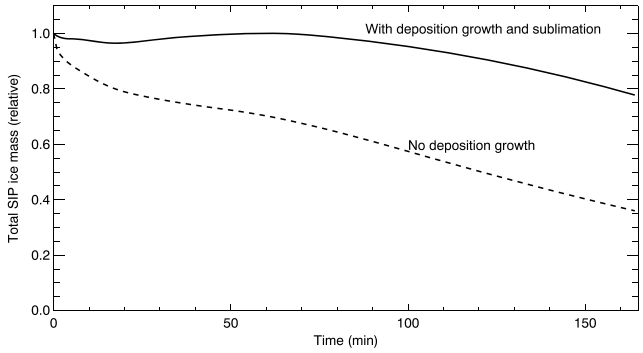

Figure 6. The evolution of total SIP ice mass (normalized to the initial value) is shown from the baseline simulation with sedimentation, deposition growth, and sublimation included (solid curve) and from a simulation with deposition growth prevented (dashed curve). Inclusion of vapor deposition growth results in a much more gradual reduction in total anvil ice mass over time than without ice crystal growth. SIP = simulated ice particles.

3. Results

As discussed above, we use the RAMS temperature, humidity, and wind fields to force the advection, sedimentation, and growth/sublimation of 200,000 ice crystals tracked in the Lagrangian framework. We refer to the SIP initialization time (1816 local time in the RAMS simulation) as zero time in the Lagrangian simulation, and the SIPs are tracked for 2.75 hr beyond this initialization time.

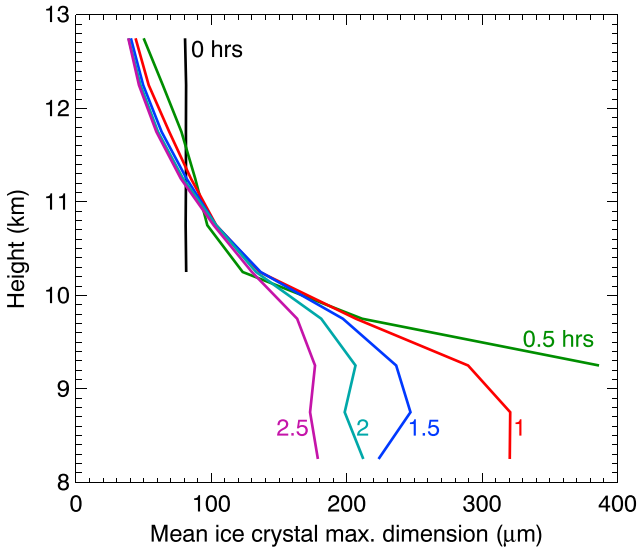

Figure 7. Average ice crystal maximum dimension height profiles (in 0.5-km height bins) are shown at 30-min intervals through the anvil life cycle.

Snapshots of the SIP sizes and locations relative to the RAMS anvil are shown at 0, 30, 60, and 150 min after initialization of the SIPs in Figure 1. The total number of SIPs surviving is indicated in each panel. Some of the SIPs are initialized just outside the supersaturated region within the RAMS anvil and sublimate rapidly. The surviving SIPs track the RAMS anvil quite well, indicating general consistency between the Lagrangian and Eulerian calculations. Some of the smaller SIPs get advected upward a few hundred meters in the residual convective updraft core. As soon as 30 min after SIP initialization, size sorting is apparent with crystals larger than ≃200 μm beginning to accumulate near the anvil cloud base (Figure 1, second row). At 2.5 hr after initialization of the SIPs, clear segregation of the ice crystals by size is apparent in both the horizontal and vertical cross sections of the anvil (Figure 1, fourth row). The combination of wind shear and gravitational size sorting results in small ice crystals dominating in the northern, higher part of the anvil, whereas larger crystals predominate in the lower, southwestern part of the anvil downwind of the updraft core.

The evolution of individual SIP heights, maximum dimensions, fall speeds and saturation ratios are shown in Figure 4. The colored curves show representative examples of the evolution of SIPs from the lower part of the detrainment zone with a range of initial maximum dimensions. Ice crystals smaller than about 100 μm (black and green curves) do not fall very far within the first few hours of anvil evolution, and it is these small crystals that dominate the anvil by number. Most of the SIPs initialized with maximum dimensions larger than about 200 μm fall into subsaturated air below the anvil and sublimate within a couple of hours. The impact of gravity wave vertical wind and temperature oscillations is apparent in the SIP heights, ice saturation ratios, and maximum dimensions. Large ice supersaturations and subsaturations driven by strong updrafts and downdrafts occur in the first 10–20 min of the simulation. Subsequently, most of the SIPs that do not fall out of the anvil encounter only modest (less than about 5%) deviations from 100% relative humidity with respect to ice.

The development of gravitational size sorting is shown by height-segregated size distributions at different times in the aging anvil (Figure 5). After about 0.5–1 hr of SIP growth and sedimentation, the size distributions show a clear dependence on height. After about 2 hr, ice crystals larger than about 300 μm are absent because the large crystals produced within the convective core have fallen out and sublimated, and deposition growth cannot produce such large crystals. Note again that aggregation is not included in these Lagrangian calculations. Observations show that many of the large ice crystals in the lower parts of anvils are aggregates (Gallagher et al., 2012). Below the lowest initial ice crystal detrainment height (≃10 km), relatively few small ice crystals are present throughout the simulation. The size distributions in the lower parts of the anvil peak at maximum dimensions greater than 200 μm, and a tail toward smaller sizes caused by ice sublimation is apparent. Small ice crystals (D < 20–30 μm) are also absent after about 2 hr in the upper part of the anvil because the initial small crystals have either grown by vapor deposition or completely sublimated. If abundant small ice crystals do exist in aged anvils, this would likely be an indication of fresh ice nucleation.

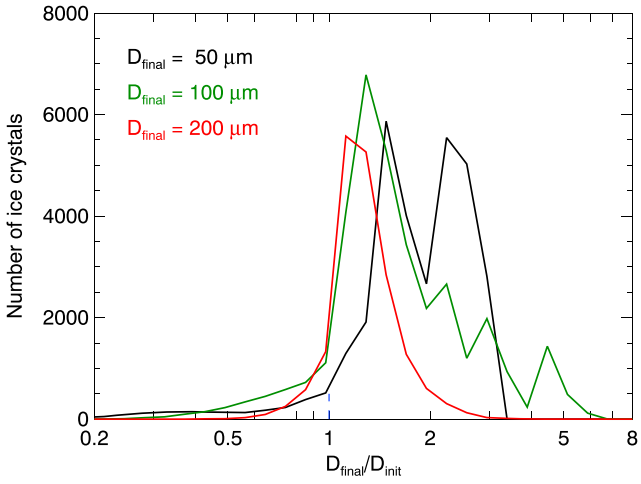

Figure 8. Ratios of ice crystal maximum dimensions at final time (2.75 hr) and initial time. The majority of ice crystals with final sizes near 50–100 μm grew substantially by deposition growth from their initial detrainment sizes.

The impact of vapor deposition growth on the total mass of the anvil as represented by the SIPs is shown in Figure 6. In a simulation with SIP deposition growth prevented (but sublimation still included), the reduction in ice mass over the ≃2.5-hr simulation is increased by about a factor of 2. Further, when deposition growth is included, the anvil ice mass remains approximately constant over the first hour rather than being depleted. These results indicate that ice crystal deposition growth is a critical process in the maintenance of the simulated anvil.

The evolution of the mean ice crystal size height profile is shown in Figure 7. Differential sedimentation dominates during the first 30 min of

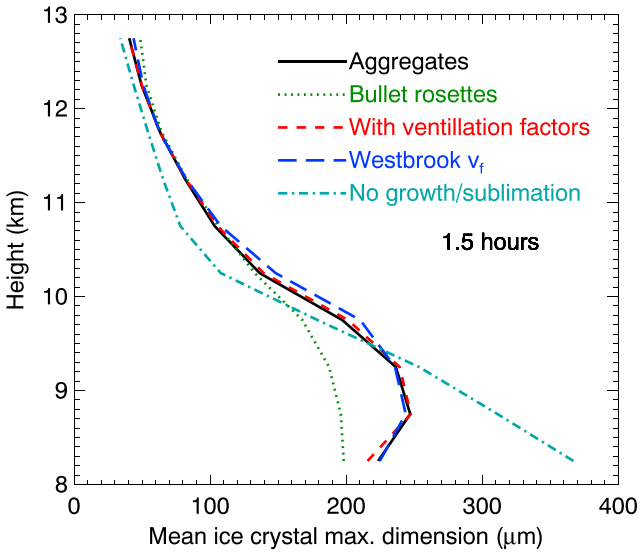

Figure 9. Average ice crystal maximum dimension height profiles are shown at 1.5 hr from simulations with different assumptions about parameters affecting ice crystal sedimentation speeds and growth rates.

the simulation, resulting in exclusively large crystals in the lower parts of the anvil and a reduction of the mean maximum dimension above about 11.5 km. Subsequently, the large ice crystals in the lower parts of the anvil sublimate, resulting in a steady decrease in mean diameter. In the upper part of the anvil (above ≃10 km), vapor deposition growth of the small crystals is approximately balanced by sedimentation removal of the larger crystals, resulting in little change in mean ice crystal size.

Growth and sublimation of SIPs in the evolving anvil are further examined by calculating the ratio of SIP maximum dimensions at the final time to the initial maximum dimensions (Figure 8). Most ice crystals with final maximum dimensions larger than about 50 μm grew by deposition of vapor, with final/initial size ratios ranging from about 1 to 5. As noted above, the observations indicating predominance of bullet rosettes in even moderately aged anvil cirrus suggest vapor deposition growth in situ in the upper troposphere, and the results here are consistent with this finding.

3.1. Impacts of Ice Crystal Terminal Fall Speed Uncertainties

As discussed in section 2.2, there are a number of uncertainties in the calculations of ice crystal terminal fall speed and vapor deposition growth rate. In particular, assumptions must be made about the ice crystal habits that affect sedimentation and growth rate dependencies on crystal maximum dimension. In the baseline Lagrangian simulation discussed above, we have used parameters in the mass- and area-dimensional power law relationships appropriate for aggregates. Images of anvil cirrus ice crystals suggest that the dominant ice habit transitions from aggregates to bullet rosettes early in the anvil life cycle. Figure 9 shows the impact of using bullet rosette habit parameters instead of aggregate parameters on the vertical profile of mean ice crystal maximum dimension at 1.5 hr. The impact of this change is negligible above the minimum initial detrainment height (10 km), but the mean ice crystal sizes are about 15% smaller in the lower, precipitation zone of the anvil. Including ventilation effects has little impact on the simulated ice crystal life cycles.

As discussed above, Westbrook (2008) calculated fall speeds of small ice crystals using a capacitance approach that predicts lower fall speeds than the Reynolds number-Best number approach (see Figure 2). The impact of using the Westbrook (2008) fall speeds for ice crystals with maximum dimensions less than 100 μm (blue curve in Figure 9) is a slight increase in mean ice crystal sizes between about 9.5 and 11 km. Overall, the general features of the anvil ice crystal life cycles are not strongly sensitive to the assumptions affecting ice crystal sedimentation rate calculations. Note that this does not imply that fully interactive simulations of convective systems and their anvils are not sensitive to fall speed uncertainties.

We have also run a simulation without deposition growth and sublimation to demonstrate the impact of these processes (blue dashed curve in Figure 9). As discussed above, sublimation removes some of the small crystals initialized in subsaturated air, whereas the ice crystals that survive in the upper part of the anvil generally grow by vapor deposition. The net impact of these processes is a slight increase in mean maximum ice dimension above about 9.6 km compared to the simulation without growth/sublimation. Below this level, ice sublimation decreases ice maximum dimensions substantially.

4. Summary and Discussion

In this study, we use growth sedimentation ice crystal trajectory calculations to investigate the life cycles of anvil ice crystals as they are advected downwind from their convective source. Temperature, water vapor, and wind fields from a CRM (RAMS) simulation of an isolated cumulonimbus cloud were used to drive the calculations. The RAMS meteorological fields were stored at 1-min intervals and then used for the Lagrangian calculations without feedback on the vapor fields calculated by RAMS. In the Lagrangian framework, 200,000 simulated ice crystals were initialized in the upper-level detrainment zone with maximum dimensions based on in situ size distribution measurements made during an aircraft transit through a convective updraft core at ≃12 km. Advection, deposition growth, and sedimentation of the simulated ice crystals were tracked over 2.75 hr.

The key results are summarized as follows:

1. Most ice crystals initialized with maximum dimensions larger than about 200 μm fall out of the anvil and sublimate in subsaturated air below within about 2 hr (Figure 4). This result is consistent with the observation that aggregates observed near convective cores are largely absent in aged anvil cirrus.
2. Clear size sorting with height caused by differential fall speeds is evident within about 30 min of anvil evolution and becomes more pronounced with time thereafter (Figure 5). In the lower parts of the mature anvil (below the main detrainment level), relatively few small ($D < 100$ μm) ice crystals are present. Since the fall speeds of small crystals are too slow to provide a source from above, the only origin of small crystals in the lower parts of the anvil is sublimation of larger crystals.
3. Vapor deposition growth accounts for about 50% of the ice mass remaining after about 2 hr (Figure 6). This result is consistent with previous arguments that dynamical support is necessary for persistence of anvil cirrus beyond a few hours.
4. Most ice crystals larger than about 50 μm after 2.75 hr of anvil evolution have substantially grown by deposition of vapor (Figure 8). The ratios of final-to-initial maximum dimensions range from 1 to 5, with a mean ratio of about 2. This result is consistent with the predominance of bullet rosette habits observed in mature anvils since bullet rosettes are formed in situ by deposition growth.
5. The ice crystal life cycle results presented here are relatively insensitive to variations in calculated ice crystal fall speeds and growth rates associated with ice crystal habit assumptions (Figure 9).

Although the results presented here support the hypothesis that deposition growth of small crystals is important for maintaining ice mass as anvil cirrus ages, we have not addressed the potential importance of fresh nucleation of ice crystals. Supersaturations large enough to drive ice nucleation would probably only occur in regions where ice concentrations and sizes are insufficient to rapidly deplete supersaturation, such as in older anvil cirrus or near the edges (particularly the tops) of the anvils. Further, the occurrence of fresh ice nucleation would depend sensitively on the mesoscale forcing (i.e., vertical motion) in the aging anvil air mass.

The importance of deposition growth (and potentially fresh ice nucleation) for persistence of anvil cirrus is consistent with observed regional differences in anvil lifetimes. In the subtropics, where prevailing subsidence would typically drive sublimation of ice crystals, anvils typically last no more than a few hours, whereas in the deep tropics, anvil cirrus can persist for up to 12 hr (Mace et al., 2006).

Inclusion of aggregation in the simulations would likely both produce larger crystals in the lower parts of the aged anvil and accelerate the removal of larger crystals from the entire anvil. We note that, at least in some aircraft measurements of aged tropical anvil cirrus, very few aggregates are apparent in the ice crystal imagery (S. Woods, personal communication, June 2017).

As noted above, radiation effects are not included in either the RAMS simulation or Lagrangian simulations presented here. Radiative heating can drive thermal instability and small-scale convection in optically thick, persistent anvil cirrus. The resulting vertical mixing could homogenize the ice crystal size distributions to some degree and potentially extend the lifetime of some of the larger crystals. The small-scale convection would also increase the likelihood of fresh ice nucleation in aging anvils. Radiative heating/cooling of individual ice crystals can also drive their surface temperature above/below the ambient temperature, thereby affecting deposition growth and sublimation rates. These radiative effects are the subject of a future study.

Acknowledgments
This work was supported by NASA's Airborne Tropical Tropopause Experiment project and by NASA grant NNX16AO93G. Data used in this study are available at the NASA Earth Science Projects Office archive (espoarchive.nasa.gov).

References

Connolly, P. J., Saunders, C. P. R., Gallagher, M. W., Bower, K. N., Flynn, M. J., Choularton, T. W., et al. (2005). Aircraft observations of the influence of electric fields on the aggregation of ice crystals. *Quarterly Journal of the Royal Meteorological Society*, *131*, 1695–1712.

Cotton, W. R., Pielke, R. A. Sr., Walko, R. L., Liston, G. E., Tremback, C. J., Jiang, H., et al. (2003). RAMS 2001: Current status and future directions. *Meteorology and Atmospheric Physics*, *82*, 5–29.

DeMott, P. J., Prenni, A. J., Liu, X., Kreidenweis, S. M., Petters, M. D., Twohy, C. H., et al. (2010). Predicting global atmospheric ice nuclei distributions and their impacts on climate. *Proceedings of the National Academy of Sciences*, *107*, 11,217–11,222.

Field, P. R., Heymsfield, A. J., & Bansemer, A. (2006). A test of ice self-collection kernels using aircraft data. *Journal of the Atmospheric Sciences*, *63*, 651–666.

Gallagher, M. W., Connolly, P. J., Crawford, I., Heymsfield, A., Bower, K. N., Choularton, T. W., et al. (2012). Observations and modelling of microphysical variability, aggregation and sedimentation in tropical anvil cirrus outflow regions. *Atmospheric Chemistry and Physics*, *12*, 6609–6628.

Grant, L. D., & van den Heever, S. C. (2014a). Aerosol-cloud-land surface interactions within tropical sea breeze convection. *Journal of Geophysical Research: Atmospheres*, *119*, 8340–8361. https://doi.org/10.1002/2014JD021912

Grant, L. D., & van den Heever, S. C. (2014b). Microphysical and dynamical characteristics of low-precipitation and classic supercells. *Journal of the Atmospheric Sciences*, *71*, 2604–2624.

Heymsfield, A. J. (1975). Cirrus uncinus generating cells and the evolution of cirriform clouds. Part II: The structure and circulations of the cirrus uncinus generating head. *Journal of the Atmospheric Sciences*, *32*, 809–819.

Heymsfield, A. J., Bansemer, A., Field, P. R., Durden, S. L., Stith, J., Dye, J. E., & Grainger, T. (1998). Observations and parameterizations of particle size distributions in deep tropical cirrus and stratiform precipitating clouds: Results from in-situ observations in TRMM field campaigns. *Journal of the Atmospheric Sciences*, *59*, 3457–3491.

Heymsfield, A. J., & Westbrook, C. D. (2010). Advances in the estimation of ice particle fall speeds using laboratory and field measurements. *Journal of the Atmospheric Sciences*, *67*, 2469–2482.

Hill, G. E. (1974). Factors controlling the size and spacing of cumulus clouds as revealed by numerical experiments. *Journal of the Atmospheric Sciences*, *31*, 646–673.

Jensen, E. J., & Ackerman, A. S. (2006). Homogeneous aerosol freezing in the tops of high-altitude tropical cumulonimbus clouds. *Geophysical Research Letters*, *33*, L08802. https://doi.org/10.1029/2005GL024928

Jensen, E. J., Lawson, P., Baker, B., Pilson, B., Mo, Q., Heymsfield, A., et al. (2009). On the importance of small ice crystals in tropical anvil cirrus. *Atmospheric Chemistry and Physics*, *9*, 5519–5537.

Kärcher, B., & Siefert, A. (2016). On homogeneous ice formation in liquid clouds. *Quarterly Journal of the Royal Meteorological Society*, *142*, 1320–1324.

Kiehl, J. T., & Ramanathan, V. (1990). Comparison of cloud forcing derived from the Earth Radiation Budget Experiment with that simulated by the NCAR Community Climate Model. *Journal of Geophysical Research*, *95*, 11,679–11,698.

Klemp, J. B., & Wilhelmson, R. B. (1978). The simulation of three-dimensional convective storm dynamics. *Journal of the Atmospheric Sciences*, *35*, 1070–1096.

Liou, K. N. (1986). Influence of cirrus clouds on weather and climate processes: A global perspective. *Monthly Weather Review*, *114*, 1167–1200.

Loftus, A. M., Weber, D. B., & Doswell, C. A. III (2008). Parameterized mesoscale forcing mechanisms for initiating numerically simulated isolated multicellular convection. *Monthly Weather Review*, *136*, 2408–2421.

Luo, Z., & Rossow, W. B. (2004). Characterizing tropical cirrus life cycle, evolution, and interaction with upper-tropospheric water vapor using Lagrangian trajectory analysis of satellite observations. *Journal of the Atmospheric Sciences*, *17*, 4541–4563.

Mace, G. G., Deng, M., Soden, B., & Zipser, E. (2006). Association of tropical cirrus in the 10–15-km layer with deep convective sources: An observational study combining millimeter radar data and satellite-derived trajectories. *Journal of the Atmospheric Sciences*, *63*, 480–503.

Massie, S., Gettelman, A., Randel, W., & Baumgardner, D. (2002). Distribution of tropical cirrus in relation to convection. *Journal of Geophysical Research*, *107*(D21), 4591. https://doi.org/10.1029/2001JD001293

Meyers, M. P., Walko, R. L., Harrington, J. Y., & Cotton, W. R. (1997). New RAMS cloud microphysics parameterization. Part II: The two-moment scheme. *Atmospheric Research*, *45*, 3–39.

Mitchell, D. L. (1996). Use of mass- and area-dimensional power laws for determining precipitation particle terminal velocities. *Journal of the Atmospheric Sciences*, *53*, 1710–1723.

Mitchell, D. L., & Heymsfield, A. J. (2005). Refinements in the treatment of ice particle terminal velocities, highlighting aggregates. *Journal of the Atmospheric Sciences*, *62*, 1637–1644.

Pruppacher, H. R., & Klett, J. D. (1997). *Microphysics of Clouds and Precipitation*. Dordrecht, Boston, London: Kluwer Academic Publishers.

Ramaswamy, V., & Detwiler, A. (1986). Interdependence of radiation and micophysics in cirrus clouds. *Journal of the Atmospheric Sciences*, *43*, 2289–2301.

Riihimaki, L. D., McFarlane, S. A., Liang, C., Massie, S. T., Beagley, N., & Toth, T. D. (2012). Comparison of methods to determine Tropical Tropopause Layer cirrus formation mechanisms. *Journal of Geophysical Research*, *117*, D06218. https://doi.org/10.1029/2011JD016832

Saleeby, S. M., & Cotton, W. R. (2004). A large-droplet mode and prognostic number concentration of cloud droplets in the Colorado State University Regional Atmospheric Modeling System (RAMS). Part I: Module descriptions and supercell test simulations. *Journal of Applied Meteorology*, *43*, 182–195.

Saleeby, S. M., & van den Heever, S. C. (2013). Developments in the CSU-RAMS aerosol model: Emissions, nucleation, regeneration, deposition, and radiation. *Journal of Applied Meteorology and Climatology*, *52*, 2601–2622.

Smagorinsky, J. (1963). General circulation experiments with the primitive equations: 1. The basic experiment. *Monthly Weather Review*, *91*, 99–164.

Sölch, S., & Kärcher, B. (2010). A large-eddy model for cirrus clouds with explicit aerosol and ice microphysics and Lagrangian ice particle tracking. *Quarterly Journal of the Royal Meteorological Society*, *136*, 2074–2093.

Stephens, G. L. (1983). The influence of radiative transfer on the mass and heat budgets. *Journal of the Atmospheric Sciences*, *40*, 1729–1739.

Toon, O. B., Starr, D. O, Jensen, E. J., Newman, P. A., Platnick, S., Schoeberl, M. R., et al. (2010). Planning, implementation, and first results of the Tropical Composition, Cloud and Climate Coupling Experiment (TC4). *Journal of Geophysical Research*, *115*, D00J04. https://doi.org/10.1029/2009JD013073

Westbrook, C. D. (2008). The fall speeds of sub-100 μm ice crystals. *Quarterly Journal of the Royal Meteorological Society*, *134*, 1243–1251.

Westbrook, C. D., Hogan, R. J., & Illingworth, A. J. (2008). The capacitance of pristine ice crystals and aggregate snowflakes. *Journal of the Atmospheric Sciences*, *65*, 206–219.

Westbrook, C. D., & Sephton, E. K. (2017). Using 3-D-printed analogues to investigate the fall speeds and orientations of complex ice particles. *Geophysical Research Letters*, *44*, 7994–8001. https://doi.org/10.1002/2017GL074130

Whiteway, J., Cook, C., Gallagher, M., Choularton, T., Harries, J., Connolly, P., et al. (2004). Anatomy of cirrus clouds: Results from the Emerald airborne campaign. *Geophysical Research Letters*, *31*, L24102. https://doi.org/10.1029/2004GL021201

Wu, T., Cotton, W. R., & Cheng, W. Y. Y. (1999). Radiative effects on the diffusional growth of ice particles in cirrus clouds. *Journal of the Atmospheric Sciences*, *57*, 2892–2904.